Research Square

Preprints are preliminary reports that have not undergone peer review.
They should not be considered conclusive, used to inform clinical practice,
or referenced by the media as validated information.

Integrated on-chip quantum light sources on a van der Waals platform

Battulga Munkhbat

bamunk@fotonik.dtu.dk

Technical University of Denmark https://orcid.org/0000-0002-1923-0960

Pietro Metuh

Technical University of Denmark https://orcid.org/0009-0003-1108-2494

Pawel Wyborski

Technical University of Denmark

Athanasios Paralikis

Technical University of Denmark,

Frederik Schröder

Technical University of Denmark

Nicolas Stenger

Technical University of Denmark

Niels Gregersen

Technical University of Denmark https://orcid.org/0000-0002-8252-8989

Article

Keywords:

Posted Date: March 12th, 2026

DOI: https://doi.org/10.21203/rs.3.rs-8748333/v1

License: This work is licensed under a Creative Commons Attribution 4.0 International License.
Read Full License

Additional Declarations: There is **NO** Competing Interest.

Integrated on-chip quantum light sources on a van der Waals platform

Pietro Metuh,[1] Paweł Wyborski,[1] Athanasios Paralikis,[1] Frederik Schröder,[1,2] Nicolas Stenger,[1,2] Niels Gregersen,[1] and Battulga Munkhbat[1,*]

[1] *Department of Electrical and Photonics Engineering, Technical University of Denmark, 2800 Kgs. Lyngby, Denmark*
[2] *NanoPhoton – Center for Nanophotonics, Technical University of Denmark, 2800 Kgs. Lyngby, Denmark*

Scalable photonic quantum information technologies require a platform combining quantum light sources, waveguides, and detectors on a single chip. Here, we introduce a van der Waals platform comprising strain-engineered bilayer WSe_2 quantum emitters, integrated on multimode WS_2 waveguides with grating couplers, enabling efficient on-chip quantum light sources. The emitters exhibit bright, highly polarised emission that couples efficiently into WS_2 waveguides. Under p-shell excitation, we observe high-purity, waveguide-coupled single-photon emission, measured using both an off-chip Hanbury Brown-Twiss configuration ($g^{(2)}(0) = 0.003^{+0.030}_{-0.003}$) and an on-chip configuration ($g^{(2)}(0) = 0.076 \pm 0.023$). For a single output, the out-coupled single-photon count rate at the first lens reaches approximately 299 kHz under continuous-wave p-shell excitation, corresponding to an estimated waveguide-coupled rate of 1.59 MHz. These results demonstrate an efficient, integrated single-photon source and establish a pathway toward scalable photonic quantum information processing centred around nanoengineered van der Waals materials.

A vision for scalable photonic quantum information processing is the realization of a quantum photonic circuit by integrating all the building blocks on a single chip.[1–3] Currently, however, state-of-the-art implementations rely on disparate material systems:[4] silicon[5,6] or silicon nitride[7] for photonic circuits, III–V semiconductors for deterministic quantum emitters,[8,9] and amorphous superconductors such as NbTiN or MoSi for single-photon detectors.[10] Integrating these components is possible in some circumstances,[11,12] but it requires complex hybrid fabrication with stringent thermal and chemical compatibility, which has become a major bottleneck for scaling up photonic quantum technologies.[4] It is therefore desirable to identify a single material platform that enables monolithic integration of all essential quantum photonic components.[13]

Transition metal dichalcogenides (TMDs) have emerged as a powerful material platform in nano- and quantum photonics owing to their versatility afforded by van der Waals (vdW) assembly.[14–16] Their stackable layered structure[17] enables combination of distinct TMDs to engineer new optical and electronic functionalities and straightforward integration with existing photonic platforms. Several mono- and bilayer TMD semiconductors, such as WSe_2[18–22] and $MoTe_2$,[23,24] can host localized quantum emitters created by strain or defect engineering,[25] producing single photons between the visible and telecom range.[26] In parallel, high nonlinear coefficients in TMDs have been exploited for enhancing nonlinearities in established material platforms.[27] Several multilayer TMDs have also high refractive indices and low absorption over a broad spectral window, supporting low-loss, tightly confined optical modes suitable for waveguides and photonic cavities,[28–31] and facilitated by their atomically smooth surfaces.[32] Beyond light sources and passive photonics, superconducting TMDs such as $NbSe_2$ have recently been explored as ultrathin single-photon detectors.[33–35] Together, these complementary features render TMDs a versatile platform for engineering emitters, circuitry, and detectors.

Despite substantial progress in developing individual vdW photonic components,[29,36–39] a complete vdW integrated circuit has not yet been realized. Previous demonstrations of vdW quantum emitters integrated into optical waveguides have shown limited coupling.[26] Monolithic integration[40,41] is hindered due to the lack of strain needed for creating quantum emitters, while hybrid waveguide structures[42,43] are limited by the thickness of TMD emitters, which is insufficient to reshape guided modes. As a consequence, demonstrations to date have relied on hybrid platforms, and no system has yet integrated TMD quantum emitters onto vdW waveguides to realize an on-chip, waveguide-coupled single-photon source.

In this work, we develop integrated quantum light sources based entirely on a nanoengineered vdW material platform. Bilayer WSe_2 quantum emitters are integrated on multimode WS_2 waveguides, enabling efficient coupling in an all-vdW emitter–waveguide system. We verify the quantum nature of a bilayer WSe_2 emitter by first using confocal detection, obtaining $g^{(2)}(0) = 0.043 \pm 0.027$. We then repeat the measurement by collecting the signal via integrated grating couplers, retaining high purity ($g^{(2)}(0) = 0.003^{+0.030}_{-0.003}$). Taking further advantage of the dual-ended waveguide, we use the waveguide itself as a beam splitter for on-chip Hanbury Brown-Twiss (HBT) measurements. High single-photon purity is preserved in this configuration ($g^{(2)}(0) = 0.076 \pm 0.023$). Moreover, we estimate an out-coupled single-photon rate at the first lens of approximately 299 kHz (223 kHz) from the first (second) grating coupler under p-shell excitation. Under the assumption of an out-coupling effi-

* bamunk@dtu.dk

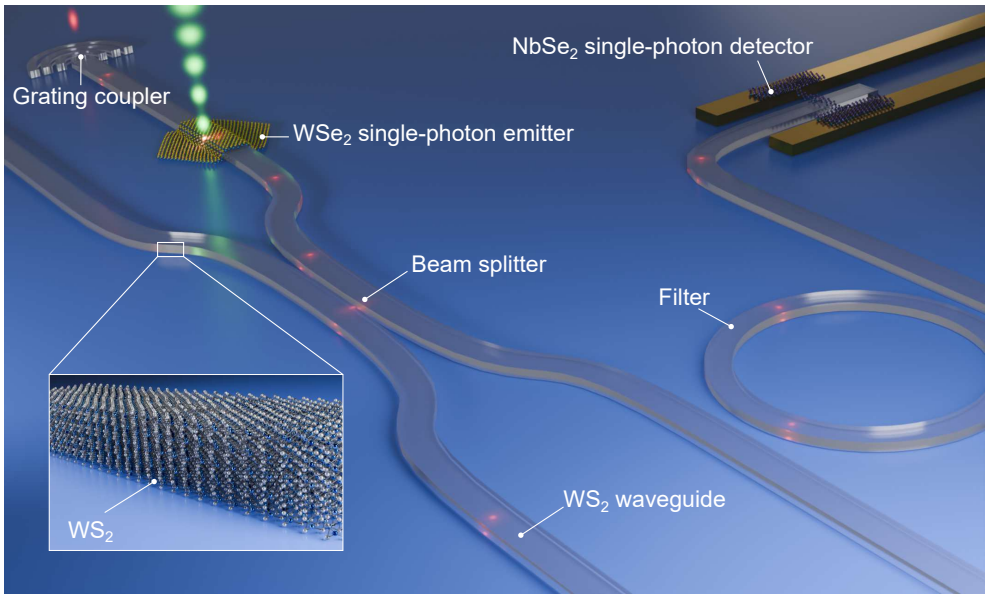


FIG. 1. **TMD-based photonic integrated circuit for scalable quantum information processing.** Distinct optical, electronic, and mechanical properties across different transition-metal dichalcogenides (TMDs) allow each material to serve a specialized function in an integrated quantum photonic architecture: mono- or bilayer WSe_2 as single-photon emitters, nanostructured multilayer WS_2 as high-index and low-loss photonic integrated circuits incorporating couplers, filters, beam splitters, and interferometers, and superconducting $NbSe_2$ nanowires as fast and efficient single-photon detectors.

ciency of 18.8%, the upper limit obtained via numerical simulations, this translates to a waveguide-coupled rate of 1.7 MHz (1.19 MHz). These results constitute the first demonstration of an integrated single-photon source where both the quantum emitter and the photonic circuitry are realized entirely from TMD materials, paving the way toward monolithic, vdW-centered quantum photonic integrated circuits.

I. Our vision: a versatile van der Waals platform for quantum photonics

Figure 1 illustrates a concept of a photonic integrated circuit made primarily of TMD materials with complementary optical and electrical functionalities.[44,45] Within this platform, strain-engineered TMDs, such as WSe_2, serve as on-demand quantum light sources. Single-photon emission has been observed in both monolayer and bilayer WSe_2, with bilayers offering reduced background photoluminescence while maintaining high brightness.[46–48] In this concept, local strain is applied by transferring WSe_2 onto slab waveguides, where edge-induced wrinkles create quantum emitters.[36,49]

Photonic circuits are realized with nanostructured multilayer TMDs, such as WS_2, which can be patterned with established nanofabrication techniques[32,50] and offer highly confined, low-loss propagation from 750 nm up to the telecom band, as required by miniaturized integrated photonics.[29] Other photonic components, such as couplers, cavities, and spectral filters, can also be implemented with the same material.[32,51] Finally, vdW superconductors, such as $NbSe_2$, can be patterned into integrated superconducting-nanowire single-photon detectors (SNSPDs),[33,34] whose detection rates, efficiency, and timing jitter excel among single-photon detector classes.

Such a platform can be developed without the need for physical or chemical vapour deposition techniques, which might limit the monolithic or hybrid fabrication of all the circuit components in a single chip. The lack of surface dangling bonds in 2D materials results in an effective integration approach,[13] where vdW films can be transferred on any photonic circuit with pre-patterned devices for generating,[37,42,49] guiding,[29,51] and detecting[33,34] single-photon states, thus making these materials compatible with existing circuit platforms.

II. Van der Waals photonic devices: waveguides and grating couplers

We begin by establishing multilayer WS_2-based optical waveguides and grating couplers as building blocks for integrated photonics. The proposed geometry consists of multimode slab waveguides ($w = 500$ nm, $h = 150$ nm), designed for large mode overlap with dipole-like emitters located near the waveguide. Figures 2a,b show the dispersion relation of the propagating modes and their electric field profile at 802 nm, respectively. Despite separating the modes into transverse-electric (TE) and transverse-magnetic (TM) depending on their primary polarisation, it is worth noting that at 802 nm most higher-order modes are hybrid, and therefore have a variable polarisation ratio. The waveguide fabrication process begins by mechanical exfoliation of WS_2 flakes. When suitable flakes at the desired thickness are found, they are transferred onto Si chips with a 2 µm SiO_2 layer and pre-patterned alignment markers. The designed structures are then fabricated by transferring an electron-beam resist pattern onto the flake via reactive-ion etching (Supplementary Note 1). The resulting waveguides are characterized by a smooth surface (given by the pristine WS_2 flake) and limited sidewall roughness or etching residues, as reported in atomic force microscopy (AFM)

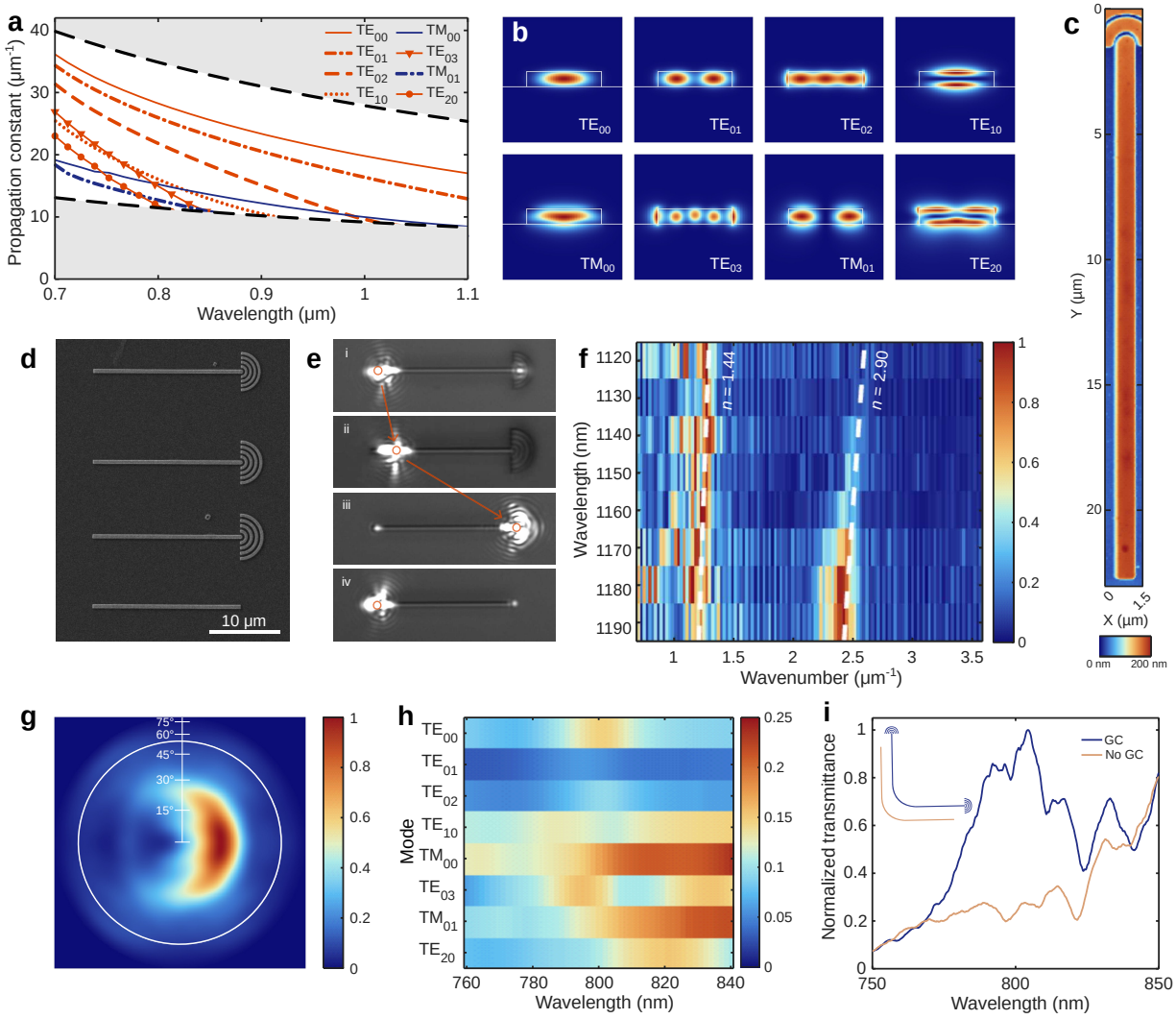


FIG. 2. **Nanostructured WS_2 for on-chip waveguides.** (a) Dispersion relation of a 500 × 150 nm WS_2 slab waveguide on a SiO_2 substrate, showing all propagating modes with a cut-off wavelength above $\lambda = 800$ nm. The dashed black lines mark the propagation constant in bulk WS_2 and SiO_2. (b) Electric field intensity profile at $\lambda = 802$ nm for each propagating mode shown in (a); the waveguide and substrate cross-sections are outlined in white. (c) Atomic force microscopy trace of the 500 × 175 nm waveguide used for near-field microscopy, showing a slab waveguide with minimal surface roughness. (d) Scanning electron microscopy image of short 500 × 150 nm waveguides with variable grating coupler design or no grating coupler (bottom waveguide). (e) Optical microscopy image of two of the waveguides shown in (d) under illumination with a broadband source; the empty orange circle indicates the beam spot. Light can be coupled in the waveguide by edge scattering (i, iv) or grating coupling (iii) and observed on the opposite end; no light is coupled by irradiating the surface of the waveguide (ii). (f) Dispersion relation of the TE modes measured with near-field microscopy (sSNOM) over the waveguide in (c) at decreasing photon wavelengths, from 1120 to 1190 nm. The two dashed lines matching the spectral features correspond to an effective refractive index of 2.90 (propagating mode) and 1.44 (SiO_2 substrate mode). (g) Far-field distribution of the upward-coupled fundamental TE mode at $\lambda = 800$ nm from the proposed grating coupler design, obtained via FDTD modelling; the light within the white circle can be collected with an objective with NA = 0.81. (h) FDTD modelling of the collection efficiency spectra for the propagating modes with the proposed grating coupler design. (i) Comparison of the total transmittance between grating coupling (blue) and side-scattering coupling (yellow) through a 60 μm-long WS_2 waveguide. The spectra are ten point-averaged and normalized by the grating-coupled transmittance value at 800 nm. The inset shows an illustration of the waveguides characterized in the measurement.

and scanning electron microscopy (SEM) images in Fig. 2c,d.

Initially, we illustrate the possible coupling mechanisms with a set of three short (21 μm) waveguides with a single-sided grating coupler, whose design is described later in this section (Fig. 2d). As shown in Fig. 2e, a broadband objective-focused beam can be launched into the waveguide by scattering through the ungrated end,

couple out of a grating coupler (as revealed by the smaller bright spot), and be collected by the same objective (i). If the beam spot is moved slightly, no light scatters through the waveguide (ii). Light can also be injected via the grated end (iii), and emission can be observed because of the up-scattered light from the opposite end. Finally, scattering from the waveguide ends enables coupling to and from a high-numerical aperture (NA) objective even without gratings (iv), despite the reduced efficiency.

To examine propagation (shown in Fig. 2c), we perform scattering-type scanning near-field optical microscopy (sSNOM) between 1120–1190 nm on a 20 µm-long waveguide (see Methods and Supplementary Fig. 2). For each wavelength, we extracted the momenta of the propagating waves.[52,53] and plotted them against the excitation wavelength to reconstruct the waveguide-mode dispersion (Fig. 2f). This revealed a mode with wavenumber $q = 2.45\ \mu\text{m}^{-1}$ at $\lambda = 1190$ nm, corresponding to an effective index $n_{\text{exp}} = 2.90$. By comparison, the simulated index of TE_{00} in a WS_2 slab waveguide with 500×175 nm in cross-section and 40 nm of over-etch on SiO_2 is $n_{\text{num}} = 2.99$, in good agreement with the sSNOM data. A second prominent feature corresponds to $n_{\text{sub}} = 1.44$, a substrate mode in the SiO_2 layer.

When probing waveguide-coupled emitters at low temperature, using a single optical path for excitation and collection via a high-NA objective is convenient to remove the need for separate fibres at each port. However, collection via an objective is less efficient than optical fibre coupling, as a fibre can be independently aligned to the phase-matched out-coupled beam.[54] In addition, typical grating designs are optimized for fibre-core dimensions and include a tapered waveguide to adiabatically alter the field confinement.[54] We therefore adopted a compact grating coupler geometry suited to vertical microscope operation, consisting of concentric half-rings.[55] The higher effective index in WS_2 compared with the referenced work,[55] which proposes a silicon-nitride coupler, causes the main deviation from the original design. The single-step etching process was maintained, thus fixing the grating depth to the waveguide height.

To maximize extraction of waveguide-coupled emission, we optimized the coupling efficiency from a guided mode to an objective with NA = 0.81 by sweeping the grating parameters in finite-difference time-domain (FDTD) simulations (Methods). The optimized coupler comprises four half-rings with a 780 nm pitch and a 55% duty cycle. Figure 2g shows the out-coupled far-field pattern for TE_{00} at 800 nm; most upward-scattered light falls within the 53.1° half-angle cone corresponding to the objective NA. The TM_{00} mode exhibits a similar pattern, which is however nearly orthogonal in polarisation to TE_{00} (Supplementary Fig. 3). Extraction-efficiency spectra (Fig. 2h) give an average of 12.5% at 802 nm across all propagating modes, with a maximum of 18.8% for TM_{00}. Efficiency is mainly limited by the high index contrast between WS_2 and air, remediable by varying the grating depth (thus requiring a two-step etching process),[54,56] and the scattering toward the substrate, which could be decreased with a suspended design or a reflective layer.[55]

Light injection through WS_2 waveguides was characterized by comparing the spectral transmittance of grated and ungrated 60 µm-long waveguides (Fig. 2i) when a focused beam entered one end and the out-coupled spectrum was measured at the opposite end. Notably, we observe a maximum around 800 nm and consistently higher transmittance between 750–850 nm with the grated structure. Extended-range spectra are provided in Supplementary Fig. 4.

III. Integration with quantum emitters

After inspecting the fabricated structures, we integrated quantum emitters on the 60 µm-long waveguide characterized in Fig. 2i by transferring a thin hexagonal boron nitride (hBN) layer onto part of the waveguide, followed by a WSe_2 bilayer. By having a thin layer of hBN between WS_2 and WSe_2, the bilayer can be transferred undamaged, while maintaining proximity between the two materials to facilitate the emitter coupling into the waveguide. The sample was then cooled to $T = 4$ K. Emitters were located by scanning a laser along the waveguide and monitoring confocal photoluminescence; once a spectral line appeared, the collection spot was repositioned to either grating to verify the emitter-waveguide coupling (Fig. 3a). Waveguide-coupled photoluminescence can also be imaged with a camera, as shown in Fig. 3b, where the laser is positioned on top of the quantum emitter characterized in Fig. 3d-g. Additional photoluminescence images are provided in Supplementary Fig. 5.

To assess how position and orientation of the emitter—modelled as a dipole source[57]—affect coupling efficiency, we performed FDTD simulations to calculate the coupling between the dipole and each propagating mode. The results show that overall TM and hybrid modes couple more strongly to the dipole because of a larger field overlap (Supplementary Note 4). Furthermore, the efficiency varies markedly with dipole orientation; Figure 3c reports the total coupling efficiency to any guided mode for each dipole orientation axis. Due to the hybrid polarisation of some propagating modes, coupling is possible not only for an in-plane dipole orthogonal to the waveguide axis (y), but also for a dipole oriented along the waveguide (x) and for an out-of-plane dipole (z), albeit with reduced efficiency. Since dipole orientation in strained WSe_2 flakes tends to follow the wrinkle direction,[22] transferring a flake onto a slab waveguide might induce emitters that are oriented along the waveguide edge. The emitter-waveguide coupling has also been modelled with a dipole along the side of the waveguide rather than above it (Supplementary Note 4).

We now focus on a spectral line at $\lambda = 802$ nm, whose emitter (QE1) lies on the excitation spot shown

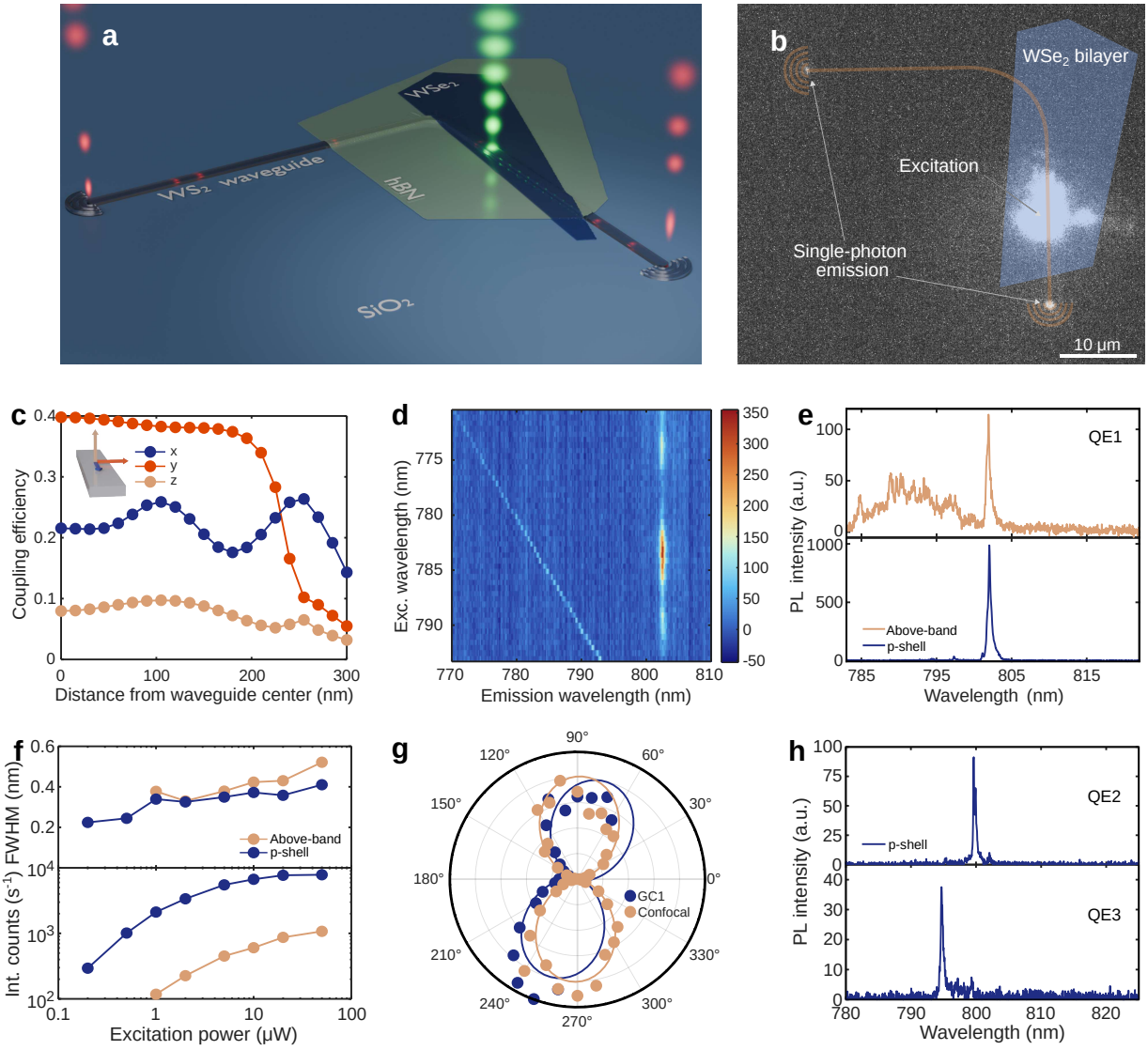


FIG. 3. **Integration of WS_2 waveguides with hBN/WSe_2 heterostructures for on-chip coupling of single photons.** (a) Artistic illustration of the characterized device, consisting of a 60 µm-long WS_2 waveguide with a 90° bend and grating couplers, with a thin (< 5 nm) hBN layer and a WSe_2 bilayer transferred on top. By optically exciting a quantum emitter in the WSe_2 bilayer, single photons couple to waveguide modes and are collected via the grating couplers. (b) Photoluminescence emitted by a laser-excited quantum emitter on bilayer WSe_2 emitter; the waveguide and a portion of the bilayer are overlapped in the image for reference. Photoluminescence is observed on both the excitation spot and the two grating couplers. (c) Simulated coupling efficiency between an electric dipole 5 nm above the waveguide and a propagating mode as a function of the distance from the vertical symmetry axis of the waveguide cross-section; the coupling is calculated with the dipole oriented along each main axis. (d) Photoluminescence excitation spectral map of a quantum emitter at $\lambda = 802$ nm, measured from GC1; the emitter can be excited via p-shell excitation, showing peak brightness with an excitation laser at $\lambda_p = 783$ nm. The partially-filtered laser line is intentionally shown. (e) Emission spectra from GC1 obtained via above-band and p-shell excitation of the quantum emitter; p-shell excitation suppresses the majority of the background emission and increases the emitter brightness. (f) Power-dependent photoluminescence (integrated counts per second at the spectrometer, logarithmic scale) and spectral linewidth of the quantum emitter at GC1 under the two excitation schemes. (g) Polarisation-dependent photoluminescence at GC1 or confocal to the excitation laser under p-shell excitation, fitted with a sinusoidal curve. (h) Additional examples of spectral lines coupled through the waveguide and collected from a grating coupler.

in Fig. 3b, and compare two excitation schemes: above-band excitation (ABE) at 650 nm and p-shell excitation (PSE), obtained by detuning the pump wavelength by 10-30 nm below the emission line, thereby still allowing efficient spectral filtering of the pump. Once a higher-energy discrete level of the emitter is reached (here, at $\lambda_p = 783$ nm), considerably brighter emission is measured both with a confocal collection spot

and at the grating couplers (Fig. 3d). Two spectra of QE1 collected at the upper grating coupler (GC1) are compared in Fig. 3e under ABE and PSE at near-saturation pump power. Brighter emission is achieved under PSE, while simultaneously reducing the spectral background from higher-energy states.[58] Both excitation schemes yield brighter waveguide-coupled photoluminescence of TMD single-photon emitters than previously reported,[36,49] which we partly attribute to a larger field overlap between the emitter and the guided modes.[26] Incidentally, bilayer WSe_2 transferred on WS_2 waveguides without a bottom hBN flake coupled more weakly (Supplementary Note 5), hinting at a role of hBN in affecting the WSe_2 charge environment.[59] The integrated counts of QE1 under PSE increased by roughly one order of magnitude at equal pump power, while the emitter linewidth is comparable to ABE, if slightly narrower (Fig. 3f and Supplementary Fig. 6). Furthermore, the decay time of this emitter is reduced from $\tau_{\mathrm{ABE}} = (55.0 \pm 1.1)$ ns to $\tau_{\mathrm{PSE}} = (31.1 \pm 0.4)$ ns (Supplementary Fig. 7).

Having established the efficacy of PSE, we evaluate additional spectral properties of waveguide-coupled WSe_2 emitters. A photoluminescence spectrogram (Supplementary Fig. 8) shows limited spectral wandering, which could be further reduced by stabilising the charge environment.[59] In addition, polarisation-resolved measurements confirm the polarised nature of the emitter, and polarisation is preserved even for waveguide-coupled emission (Fig. 3g and Supplementary Fig. 9). The degree of linear polarisation (DOLP), calculated as $(I_{\max} - I_{\min})/(I_{\max} + I_{\min})$, at GC1 and confocal to the emitter gives $(84 \pm 18)\%$ and $(98^{+2}_{-8})\%$, respectively, similarly to other strain-engineered WSe_2 emitters.[22] The polarisation aligns with the waveguide in the confocal case, implying that the dipole has a component parallel to the waveguide. However, an out-of-plane component cannot be excluded, since its emission would be largely inaccessible under confocal collection yet could still couple to a waveguide mode. Both dipole orientations couple most efficiently with TM or hybrid modes. In addition, since the out-coupled polarisation at the grating couplers matches the simulated field distribution of a TM mode (Supplementary Fig. 2), we conclude that a TM-polarised waveguide mode is the main contributor to the measured signal.

Finally, to further demonstrate the fabrication of waveguide-coupled quantum emitters with this method, we report additional bright lines between 795 and 800 nm from other emitters (Fig. 3h) under p-shell excitation and collection at a grating coupler, confirming that WS_2 waveguides constitute a robust platform for on-chip coupling of vdW emitters.

IV. On-chip second-order correlation measurement

To verify the single-photon nature of QE1, we evaluated the second-order autocorrelation function $g^2(\tau)$ under different HBT configurations. First, single photons are collected confocally from the excitation spot (Fig. 4a). The signal is then split into two arms with a beam splitter and correlated after detection with an SNSPD, producing the autocorrelation trace shown in Fig. 4d. The fitted curve yields a zero-delay second-order correlation of $g^{(2)}(0) = 0.043 \pm 0.027$, demonstrating the high single-photon purity of QE1.

The measurement is repeated by moving the collection spot to GC1 (Fig. 4b), thereby correlating the waveguide-coupled emission. With this dataset, the purity of the single-photon state ($g^{(2)}(0) = 0.003^{+0.030}_{-0.003}$) increases further, approaching the unity limit. We attribute the increased purity from the confocal configuration to a slightly lower excitation power and to more efficient waveguide coupling of the emitter compared with background emission.

In the final configuration, the beam splitter in the HBT setup is removed, and a second collection spot is implemented and aligned with the other grating coupler, GC2 (Fig. 4c), so that the waveguide itself is used as an on-chip beam splitter. In addition to simplifying the experimental setup, this improves the robustness of the second-order autocorrelation measurement, which is obtained by correlating photons at two separate waveguide ports, rather than halving the photon stream from a single port. The resulting measurement confirms the preserved purity of the quantum emitter ($g^{(2)}(0) = 0.076 \pm 0.023$) and provides, to our knowledge, the first demonstration of an HBT measurement of vdW quantum emitters using on-chip waveguides and beam splitters. The whole autocorrelation traces and raw $g^{(2)}(0)$ values are presented in Supplementary Note 6.

We conclude by discussing the emitter brightness. The single-photon count rate at saturation measured by the SNSPD during the HBT measurement yielded approximately 20 and 15 kHz for GC1 and GC2, respectively. Accounting for the losses in the transmission setup, we estimated the single-photon rate at the first lens to be 299 and 223 kHz for the respective grating coupler. Since the maximum theoretical extraction efficiency from the grating coupler is 18.8%, as shown in Fig. 2h, we estimate a minimum waveguide-coupled single-photon rate of 1.59 MHz and 1.19 MHz along the two directions. We note that this is a conservative estimation, as fabrication imperfections and multimode coupling render the simulated extraction efficiency value an upper bound. In comparison, the confocal count rate at the first lens is evaluated at 1.49 MHz. Given an average re-excitation time of 31.1 ns (from the measured decay time), the total waveguide-coupled quantum efficiency is estimated at 10%, highlighting the effective coupling mechanism in the presented vdW system. Details about the single-photon rates and efficiency figures are provided in Supplementary Note 7. Further improvements could be achievable by increasing spectral stability via electrical biasing. In addition, the emitter brightness and indistinguishability could be enhanced by integration with high-Q optical

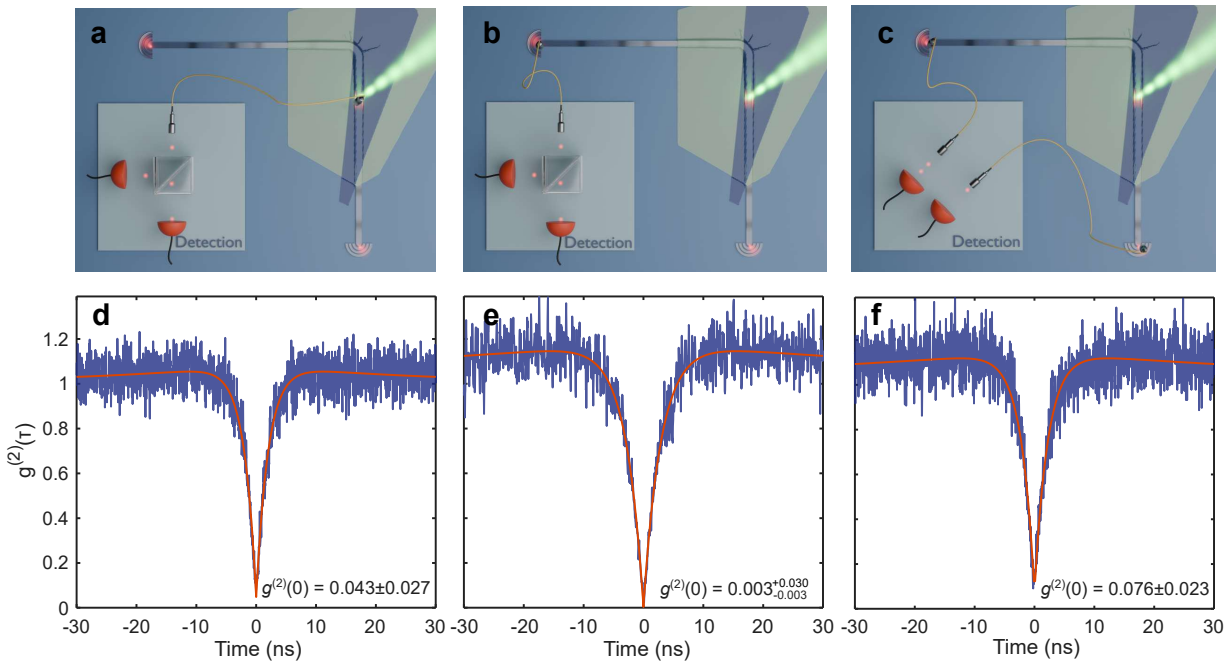


FIG. 4. **On-chip waveguide-coupled single-photon purity.** (a-c) Simplified illustration of the Hanbury Brown and Twiss (HBT) experimental setup realized with (a) the collection spot confocal to the excitation source and an external beam splitter before the detectors; (b) the collection spot at one grating coupler with an external beam splitter before the detectors; (c) a collection spot at each grating coupler, so that the HBT effect can be observed without an external beam splitter. (d-f) Continuous-wave second-order autocorrelation traces obtained with the respective setup; the traces are plot with a three-point moving average, and show signatures of photoluminescence blinking. All configuration exhibit high single-photon purity at zero time delay.

cavities[40,60,61] and advanced excitation schemes.[48,62]

V. Conclusions

In this work, we demonstrated integrated quantum emitters built entirely on a van der Waals platform. The integration of bilayer WSe_2 quantum emitters with multimode WS_2 waveguides enabled efficient on-chip coupling of high-purity, polarised single photons. Multiple single-photon emitters were shown to couple efficiently to WS_2 waveguides, highlighting the robustness of the platform. Moreover, the bidirectional coupling of the WS_2 waveguide was exploited to establish an on-chip second-order correlation experiment. The estimated MHz-level waveguide-coupled single-photon rates indicate efficient emitter-waveguide coupling and underscore the potential of the vdW platform for bright integrated sources. Looking ahead, extending this platform with single-photon detectors, phase modulators, and interferometric components would enable a promising route to vdW quantum photonic integrated circuits, paving the way for scalable quantum information processing based entirely on nano-engineered two-dimensional materials.

Methods

A. Numerical modelling

Eigenmode modelling. Modelling of the propagating modes and the dispersion relation were carried out with a finite-difference eigenmode solver in Ansys Lumerical. For the calculations, a dispersive complex refractive index was fitted for each material; for WS_2, an anisotropic index was implemented.[45]

Grating coupler simulations. The design of the grating coupler and the calculations of waveguide-objective coupling, far-field maps, and dipole-waveguide coupling were simulated with the FDTD solver in Ansys Lumerical. The initial structure of the grating coupler was adopted by another work[55] and optimized by sweeping ring period, duty cycle (i.e., the ratio between the ring width and the ring period), and number of rings. The out-coupling efficiency, which is the product of the upward-scattered transmittance from the grating with the fraction of the far field within the objective aperture, was calculated by calculating the transmittance from each propagating mode to a field monitor above the grating coupler; the transmittance was then integrated within the light cone of an objective with NA = 0.81, corresponding to a half-angle of about 53.1°.

Dipole-waveguide coupling simulations. Dipole-

waveguide simulations were modelled in Ansys Lumerical by calculating the projection of each propagating mode in the transmittance from a dipole source into the slab waveguide. Due to the variable dipole power emitted by the source (which is highly dependent on the dipole position relative to the waveguide), the coupling efficiency was normalized by the Purcell factor at each position, so that the coupling relative to the real emitted power can be evaluated.[57] Unless otherwise stated, the dipole was positioned 5 nm above the waveguide to mimic the hBN thickness. The total coupling efficiency is calculated by summing the contribution of all eight propagating modes for each dipole axis orientation.

B. Nanofabrication

Substrate preparation. The substrates are prepared by thermally growing 2 µm of SiO_2 on silicon and patterning alignment markers with a negative UV resist (AZ nLOF 2020) and electron-beam evaporation of 5 nm of titanium, followed by 50 nm of gold. The metal is lifted off in an ultrasonic bath of MICROPOSIT Remover 1165 and rinsed in isopropyl alcohol and water.

Exfoliation and transferring. WS_2, hBN, and WSe_2 (HQ Graphene) are exfoliated using the same stamping technique.[17] Semiconductor wafer tape (Nitto SWT 20+R) is used to initially exfoliate and thin down large flakes from a bulk crystal. Polydimethylsiloxane (PDMS) stamps on glass slides are then used to exfoliate the crystal into smaller flakes, which are selected by thickness and homogeneity. The thickness of WS_2 flakes was measured with the transfer matrix method by fitting reflectivity spectra from confocal illumination of the flake on the PDMS stamp with a broadband source. Thin flakes of hBN were selected by their optical contrast under an optical microscope, and bilayer WSe_2 was identified by room-temperature photoluminescence with a blue LED.

WS_2 flakes are positioned and transferred onto the substrate with a transfer station (HQ Graphene Systems HQ2D MAN), where the substrate is heated to 70°C to overcome the adhesion of the flake to PDMS upon contact. Three baths of acetone, isopropyl alcohol, and deionized water are used to clean the sample from contaminants at the end of the transfer process. After transferring the flakes, the fit was confirmed with a stylus profilometer (Bruker Dektak XTA). The same method has been used to transfer hBN and WSe_2 after patterning the waveguides and removing the resist mask.

Patterning of WS_2 waveguides. WS_2 flakes were patterned with electron-beam lithography by spin coating an adhesion promoter (Microchemicals TI Prime) and negative resist (Allresist AR-N 7520) and exposing it (Raith eLINE at 30 kV or JEOL JBX-9500FS at 100 kV). A thin aluminium layer (10 nm) was thermally evaporated on the samples processed at 100 kV before the exposure. Aluminium was removed with AZ 726 MIF (2.38% tetramethylammonium hydroxide) in 30 s and rinsed in water, while the resist was developed with Allresist AR 300-47 in 1 min and rinsed in water. The resist was descummed in an oxygen plasma for 30 s. The pattern was transferred to the WS_2 flake with an ICP-RIE tool (SPS M/PLEX ICP–RIE) in a CHF_3- and Ar-based chemistry (40 sccm flow for each gas, 10 mTorr pressure, 150 W coil power and 25 W platen power), and the resist is removed with an oxygen plasma.

C. Characterization

Near-field measurements. A scattering-type scanning near-field optical microscope (attocube neaSCOPE) in reflection mode was used to map a 500×175 nm WS_2 slab waveguide with 50 nm of SiO_2 overetch. The incident light from a tunable laser (Sacher Lasertechnik Group TEC-520-1180-030) is focused by a parabolic mirror on a platinum–iridium coated silicon AFM probe tip (NanoWorld ARROW-NCPt) operating in tapping mode. The excitation light impinges in the YZ plane (see Fig. 2c) at an angle of approximately 45°. The scattered light is detected with a photodiode (Newport 2053-FC). Both the excitation and the scattered light are filtered with co-polarised linear polarisers, aligned in s-polarisation. The signal recorded by the photodiode is demodulated at the third harmonic order of the tip tapping frequency.[63,64] Together with a pseudo-heterodyne detection scheme,[65] this allows retrieval of the near-field amplitude while the far-field signal is largely suppressed.

Waveguide characterization. Room-temperature coupling to the waveguide was performed with a homemade confocal photoluminescence setup by using a filtered broadband source (Thorlabs OSL2IR) coupled to a single-mode fiber (Thorlabs P3-780A-FC-2), a 50× objective (Nikon LU Plan Fluor, NA = 0.8), and an infrared spectrometer (Andor Kymera 328i, Andor iDus InGaAs 1.7 µm). The sample was imaged with a CMOS camera (Thorlabs CS165MU/M).

For low-temperature characterization measurements, the sample was loaded in an optical, closed-cycle vacuum cryostat (attocube attoDRY800) with a nano-positioner and a base temperature of $T \approx 4$ K. At low temperature, the transmission measurements were carried out with the same light source, but with a visible-light spectrometer (Horiba iHR 550, Horiba Syncerity BI-NIR) and imaging camera (Tucsen Dhyana 400D). A low-temperature objective (attocube LT-APO/NIR/0.81, NA = 0.81) is used to focus the light on the sample surface. The spectra were post-processed with a ten-point moving average to smoothen the signal, and are normalized by dividing the traces with a reference spectrum of a reflective gold mirror.

Photoluminescence measurements. Bilayer WSe_2 is illuminated with either a 650-nm diode laser (PicoQuant LDH-D-C-650) in continuous-wave or pulsed mode for above-band excitation, a tunable (770-795 nm)

CW laser (Toptica DL PRO) for continuous-wave p-shell excitation, and a tunable femtosecond laser (Coherent Chameleon Ultra II) for pulsed p-shell excitation. The laser polarisation is controlled with a half-wave plate and a linear polariser before entering the optical window of the cryostat and is focused by the same low-temperature objective. The same objective collimates the photoluminescence signal, which is filtered from the laser pump with different configurations of bandpass or longpass filters. The detection polarisation is controlled with a half-wave plate and a linear polariser before coupling to a single-mode fibre. Photoluminescence mapping was performed with the camera and the spectrometer mentioned above.

The polarisation-resolved measurements were fitted with the following function:

$$I(\phi) = a\sin^2(\phi - \phi_0) + b. \tag{1}$$

The error in the degree of linear polarisation, calculated as $a/(a+2b)$, is given as a 95% confidence interval and is calculated by propagating the error from (1).

Decay time and second-order correlation measurements. Time-correlation measurements were carried out by detecting the signal using a superconducting nanowire single-photon detector (ID Quantique ID281). Temporal events for time-resolved photoluminescence and second-order autocorrelation measurements were correlated with a time-to-digital converter (Swabian Instruments Time Tagger Ultra).

All second-order correlations were measured with the tunable CW laser at $\lambda_p = 783$ nm. The presented raw data are processed with a three-point average. The fitting was carried out with a three-level model, which is described by the following equation:[66]

$$g^{(2)}(\tau) = 1 - (1+a)e^{-|\tau|/\tau_1} + be^{-|\tau|/\tau_2}, \tag{2}$$

where τ_1 and τ_2 are antibunching- and bunching-related time constants, respectively. The error in the second-order correlation at zero delay is given as a 95% confidence interval, and is calculated as a sum of the errors of a and b.

Sample imaging. Optical microscopy images were taken in confocal microscopes with various objectives and cameras. The topography of the photonic circuits and of the transferred hBN and WSe_2 was characterized with a scanning electron microscope (Zeiss Supra 40 VP, 5 kV, SE2 detector) and an atomic force microscope (Bruker Dimension Icon, tapping mode with Tap150Al-G tips). Samples containing bilayer WSe_2 flakes were imaged only at the sample end-of-life to avoid inducing defects or charging the bilayer before characterization.

Acknowledgements

P.M., P.W., A.P., N.G., and B.M. acknowledge support from the European Research Council (ERC-StG "TuneTMD", grant no. 101076437) and Villum Fonden (project no. VIL53033). The authors also acknowledge the European Research Council (ERC-CoG "Unity", grant no. 865230), the TICRA foundation, the Innovation Fund Denmark (QLIGHT, no. 4356-00002A), and the cleanroom facilities at the Danish National Centre for Nano Fabrication and Characterization (DTU Nanolab). F.S. and N.S. are supported by the Danish National Research Foundation through NanoPhoton—Center for Nanophotonics, Grant No. DNRF147. N.S. acknowledges funding by the Novo Nordisk Foundation NERD Programme (Project QuDec NNF23OC0082957). Finally, P.M. acknowledges Ryo Mizuta Graphics for the Optical Components Pack asset, which was partially used for the artistic illustrations in Fig. 4.

Author contribution

P.M. performed the numerical modelling, fabricated the waveguides, and processed and analyzed all the presented data. F.S. performed the sSNOM characterization, supervised by N.S. A.P. and P.M. transferred the hBN/WSe_2 stacks on the waveguides. P.W. and P.M. performed the optical characterization of the waveguides and the quantum emitters. B.M. supervised and coordinated the project. P.M., P.W., A.P., and B.M. wrote the manuscript with input from all co-authors.

Competing Interests

The authors declare they have no competing interests.

Data availability statement

The data supporting the findings of this study are available within the main manuscript and its supplementary information files. Additional data are available from the corresponding authors upon reasonable request.

References

[1] O'Brien, J. L., Furusawa, A. & Vučković, J. Photonic quantum technologies. *Nature Photon* **3**, 687–695 (2009).

[2] Zhong, H.-S. *et al.* Quantum computational advantage using photons. *Science* **370**, 1460–1463 (2020).

[3] Wang, H. *et al.* Toward Scalable Boson Sampling with Photon Loss. *Phys. Rev. Lett.* **120**, 230502 (2018).

[4] Pelucchi, E. *et al.* The potential and global outlook of integrated photonics for quantum technologies. *Nat Rev Phys* **4**, 194–208 (2021).

[5] Paesani, S. *et al.* Near-ideal spontaneous photon sources in silicon quantum photonics. *Nat Commun* **11**, 2505 (2020).

[6] Silverstone, J. W., Bonneau, D., O'Brien, J. L. & Thompson, M. G. Silicon Quantum Photonics. *IEEE Journal of Selected Topics in Quantum Electronics* **22**, 390–402 (2016).

[7] Wang, Y. *et al.* Deterministic photon source interfaced with a programmable silicon-nitride integrated circuit. *npj Quantum Inf* **9**, 94 (2023).

[8] Senellart, P., Solomon, G. & White, A. High-performance semiconductor quantum-dot single-photon sources. *Nature Nanotech* **12**, 1026–1039 (2017).

[9] Ding, X. *et al.* High-efficiency single-photon source above the loss-tolerant threshold for efficient linear optical quantum computing. *Nat. Photon.* **19**, 387–391 (2025).

[10] Esmaeil Zadeh, I. *et al.* Superconducting nanowire single-photon detectors: A perspective on evolution, state-of-the-art, future developments, and applications. *Applied Physics Letters* **118**, 190502 (2021).

[11] Schwartz, M. *et al.* Fully On-Chip Single-Photon Hanbury-Brown and Twiss Experiment on a Monolithic Semiconductor-Superconductor Platform. *Nano Letters* **18**, 6892–6897 (2018). 1806.04099.

[12] Reithmaier, G. *et al.* On-chip time resolved detection of quantum dot emission using integrated superconducting single photon detectors. *Sci Rep* **3**, 1901 (2013).

[13] Turunen, M. *et al.* Quantum photonics with layered 2D materials. *Nat Rev Phys* **4**, 219–236 (2022).

[14] Zotev, P. G. *et al.* Nanophotonics with multilayer van der Waals materials. *Nat. Photon.* **19**, 788–802 (2025).

[15] Montblanch, A. R., Barbone, M., Aharonovich, I., Atatüre, M. & Ferrari, A. C. Layered materials as a platform for quantum technologies. *Nature Nanotechnology 2023 18:6* **18**, 555–571 (2023).

[16] Azimi, A. *et al.* Photonics in Flatland: Challenges and opportunities for nanophotonics with 2D semiconductors. *npj Nanophoton.* **2**, 44 (2025).

[17] Castellanos-Gomez, A. *et al.* Deterministic transfer of two-dimensional materials by all-dry viscoelastic stamping. *2D Mater.* **1**, 011002 (2014).

[18] Koperski, M. *et al.* Single photon emitters in exfoliated WSe2 structures. *Nature Nanotechnology 2015 10:6* **10**, 503–506 (2015). 1411.2774.

[19] Barbone, M. *et al.* Charge-tuneable biexciton complexes in monolayer WSe2. *Nat Commun* **9**, 3721 (2018).

[20] Parto, K., Azzam, S. I., Banerjee, K. & Moody, G. Defect and strain engineering of monolayer WSe2 enables site-controlled single-photon emission up to 150 K. *Nature Communications* **12** (2021).

[21] Drawer, J.-C. *et al.* Monolayer-Based Single-Photon Source in a Liquid-Helium-Free Open Cavity Featuring 65% Brightness and Quantum Coherence. *Nano Lett.* **23**, 8683–8689 (2023).

[22] Paralikis, A. *et al.* Tailoring polarization in WSe2 quantum emitters through deterministic strain engineering. *npj 2D Mater Appl* **8**, 1–8 (2024).

[23] Zhao, H., Pettes, M. T., Zheng, Y. & Htoon, H. Site-controlled telecom-wavelength single-photon emitters in atomically-thin MoTe2. *Nature Communications 2021 12:1* **12**, 1–7 (2021).

[24] Wyborski, P. *et al.* Toward triggered generation of indistinguishable single-photons from MoTe2 quantum emitters (2025). 2508.20743.

[25] Linhart, L. *et al.* Localized Intervalley Defect Excitons as Single-Photon Emitters in WSe2. *Physical Review Letters* **123** (2019). 1904.03217.

[26] Michaelis de Vasconcellos, S. *et al.* Single-Photon Emitters in Layered Van der Waals Materials. *physica status solidi (b)* **259**, 2100566 (2022).

[27] Wang, Y. *et al.* Enhancing Si3N4 Waveguide Nonlinearity with Heterogeneous Integration of Few-Layer WS2. *ACS Photonics* **8**, 2713–2721 (2021).

[28] Ling, H., Li, R. & Davoyan, A. R. All van der Waals Integrated Nanophotonics with Bulk Transition Metal Dichalcogenides. *ACS Photonics* **8**, 721–730 (2021).

[29] Vyshnevyy, A. A. *et al.* Van der Waals Materials for Overcoming Fundamental Limitations in Photonic Integrated Circuitry. *Nano Letters* **23**, 8064 (2023).

[30] Lee, S. W., Lee, J. S., Choi, W. H. & Gong, S. H. Ultrathin WS2 Polariton Waveguide for Efficient Light Guiding. *Advanced Optical Materials* **11**, 2300069 (2023).

[31] Moore, S. L. *et al.* Van der Waals waveguide quantum electrodynamics probed by infrared nanophotoluminescence. *Nat. Photon.* (2025).

[32] Munkhbat, B., Küçüköz, B., Baranov, D. G., Antosiewicz, T. J. & Shegai, T. O. Nanostructured Transition Metal Dichalcogenide Multilayers for Advanced Nanophotonics. *Laser and Photonics Reviews* **17** (2023). 2202.04898.

[33] Metuh, P. *et al.* Toward Single-Photon Detection with Superconducting Niobium Diselenide Nanowires. *ACS Photonics* **12**, 5912–5920 (2025).

[34] Zugliani, L. *et al.* 1 Single-photon detection in atomically thin NbSe2 superconducting nanowires .

[35] Wang, H. *et al.* Emerging Single-Photon Detectors Based on Low-Dimensional Materials. *Small* **18**, 2103963 (2022).

[36] Errando-Herranz, C. *et al.* Resonance Fluorescence from Waveguide-Coupled, Strain-Localized, Two-Dimensional Quantum Emitters. *ACS Photonics* **8**, 1069–1076 (2021). 2002.07657.

[37] Blauth, M. *et al.* Coupling Single Photons from Discrete Quantum Emitters in WSe2 to Lithographically Defined Plasmonic Slot Waveguides. *Nano Lett.* **18**, 6812–6819 (2018).

[38] Huang, X. *et al.* On-chip integrated light sources with MoS2/WSe2 moiré superlattices at telecom wavelengths (2025). 2504.03267.

[39] Gérard, D. *et al.* Top-down integration of an hBN quantum emitter in a monolithic photonic waveguide. *Appl.*

Phys. Lett. **122**, 264001 (2023).

[40] Kim, S. *et al.* Photonic crystal cavities from hexagonal boron nitride. *Nat Commun* **9**, 2623 (2018).

[41] Khelifa, R. *et al.* WSe2 Light-Emitting Device Coupled to an h-BN Waveguide. *ACS Photonics* **10**, 1328–1333 (2023).

[42] Tonndorf, P. *et al.* On-Chip Waveguide Coupling of a Layered Semiconductor Single-Photon Source. *Nano Lett.* **17**, 5446–5451 (2017).

[43] Kim, S. *et al.* Integrated on Chip Platform with Quantum Emitters in Layered Materials. *Advanced Optical Materials* **7**, 1901132 (2019).

[44] Manzeli, S., Ovchinnikov, D., Pasquier, D., Yazyev, O. V. & Kis, A. 2D transition metal dichalcogenides. *Nat Rev Mater* **2**, 17033 (2017).

[45] Munkhbat, B., Wróbel, P., Antosiewicz, T. J. & Shegai, T. O. Optical Constants of Several Multilayer Transition Metal Dichalcogenides Measured by Spectroscopic Ellipsometry in the 300–1700 nm Range: High Index, Anisotropy, and Hyperbolicity. *ACS Photonics* **9**, 2398–2407 (2022).

[46] Desai, S. B. *et al.* Strain-Induced Indirect to Direct Bandgap Transition in Multilayer WSe2. *Nano Lett.* **14**, 4592–4597 (2014).

[47] Kumar, S., Kaczmarczyk, A. & Gerardot, B. D. Strain-Induced Spatial and Spectral Isolation of Quantum Emitters in Mono- and Bilayer WSe2. *Nano Lett.* **15**, 7567–7573 (2015).

[48] Piccinini, C. *et al.* High-purity and stable single-photon emission in bilayer WSe2 via phonon-assisted excitation. *Commun Phys* **8**, 158 (2025).

[49] Peyskens, F., Chakraborty, C., Muneeb, M., Van Thourhout, D. & Englund, D. Integration of single photon emitters in 2D layered materials with a silicon nitride photonic chip. *Nat Commun* **10**, 4435 (2019).

[50] Munkhbat, B. *et al.* Transition metal dichalcogenide metamaterials with atomic precision. *Nature Communications* **11** (2020). 2002.05696.

[51] Ling, H. *et al.* Deeply subwavelength integrated excitonic van der Waals nanophotonics. *Optica, Vol. 10, Issue 10, pp. 1345-1352* **10**, 1345–1352 (2023).

[52] Casses, L. N., Kaltenecker, K. J., Xiao, S., Wubs, M. & Stenger, N. Quantitative near-field characterization of surface plasmon polaritons on monocrystalline gold platelets. *Opt. Express, OE* **30**, 11181–11191 (2022).

[53] Casses, L. N. *et al.* Full Quantitative Near-Field Characterization of Strongly Coupled Exciton–Plasmon Polaritons in Thin-Layered WSe2 on a Monocrystalline Gold Platelet. *ACS Photonics* **11**, 3593–3601 (2024).

[54] Cheng, L., Mao, S., Li, Z., Han, Y. & Fu, H. Y. Grating couplers on silicon photonics: Design principles, emerging trends and practical issues. *Micromachines* **11** (2020).

[55] Zhu, Y. *et al.* Ultra-compact silicon nitride grating coupler for microscopy systems. *Opt. Express* **25**, 33297 (2017).

[56] Chen, X., Li, C. & Tsang, H. K. Fabrication-Tolerant Waveguide Chirped Grating Coupler for Coupling to a Perfectly Vertical Optical Fiber. *IEEE Photonics Technology Letters* **20**, 1914–1916 (2008).

[57] Wang, Y. J., Vannucci, L., Burger, S. & Gregersen, N. Near-unity efficiency in ridge waveguide-based, on-chip single-photon sources. *Mater. Quantum. Technol.* **2**, 045004 (2022).

[58] Mitryakhin, V. N. *et al.* Rabi oscillations of a monolayer quantum emitter driven through its excited state (2025). 2510.23222.

[59] Paralikis, A., Wyborski, P., Metuh, P., Gregersen, N. & Munkhbat, B. Tunable and Low-Noise WSe2 Quantum Emitters for Quantum Photonics. *PRX Quantum* **6**, 040339 (2025).

[60] Iff, O. *et al.* Purcell-Enhanced Single Photon Source Based on a Deterministically Placed WSe2 Monolayer Quantum Dot in a Circular Bragg Grating Cavity. *Nano Lett.* **21**, 4715–4720 (2021).

[61] Binkowski, F. *et al.* High Purcell enhancement in all-TMDC nanobeam resonator designs with active monolayers for nanolasers. *Phys. Rev. B* **112**, 235410 (2025).

[62] Vannucci, L. *et al.* Single-photon emitters in WSe 2 : Critical role of phonons on excitation schemes and indistinguishability. *Phys. Rev. B* **109**, 245304 (2024).

[63] Raschke, M. B. & Lienau, C. Apertureless near-field optical microscopy: Tip–sample coupling in elastic light scattering. *Appl. Phys. Lett.* **83**, 5089–5091 (2003).

[64] Knoll, B. & Keilmann, F. Enhanced dielectric contrast in scattering-type scanning near-field optical microscopy. *Optics Communications* **182**, 321–328 (2000).

[65] Ocelic, N., Huber, A. & Hillenbrand, R. Pseudoheterodyne detection for background-free near-field spectroscopy. *Appl. Phys. Lett.* **89**, 101124 (2006).

[66] Rodiek, B. *et al.* Experimental realization of an absolute single-photon source based on a single nitrogen vacancy center in a nanodiamond. *Optica* **4**, 71–76 (2017).

Supplementary Files

This is a list of supplementary files associated with this preprint. Click to download.

- SupplementaryMaterials.pdf